Journal of Materials Research and Technology 33 (2024) 600–611

Contents lists available at ScienceDirect

Journal of Materials Research and Technology

journal homepage: www.elsevier.com/locate/jmrt

Breaking the strength-ductility trade-off in austenitic stainless steel at cryogenic temperatures: Mechanistic insights

Digvijay Singh, Fumiyoshi Yoshinaka, Susumu Takamori, Satoshi Emura, Takahiro Sawaguchi *

National Institute for Materials Science, 1-2-1 Sengen, Tsukuba, Ibaraki, 305-0047, Japan

ARTICLE INFO

Keywords:
Strength-ductility balance
Austenitic stainless steel
Martensitic transformation
Deformation twinning
Strain-hardening rate

ABSTRACT

At cryogenic temperatures, 316L austenitic stainless steel (ASS) exhibits remarkable strength while retaining high ductility, defying the conventional stress-strain trade-off. Despite extensive studies documenting the cryo-tensile properties of ASSs, the underlying mechanisms behind this phenomenon remain largely unexplored. This study systematically re-examines the tensile properties of 316L stainless steel and the associated mechanisms across a range of low temperatures (293 K, 223 K, 123 K, and 77 K). The reasons for the superior stress-strain balance (~80 % GPa) are discussed using results from electron backscatter diffraction (EBSD) microstructure characteristics. The results undoubtedly suggest that the transformation mechanisms, specifically the shift from deformation twinning to martensitic transformation ($\gamma \rightarrow \varepsilon \rightarrow \alpha'$), play a crucial role in enhancing elongation at cryogenic temperatures. At these temperatures, the Gibbs free energy difference between ε-martensite and γ-austenite approaches zero, resulting in slow martensite growth. The stress-strain curves at low temperatures satisfy the Considère criterion, indicating delayed necking under these conditions. This behavior is ascribed to the presence of various hierarchical microstructures, including ε, α', γ-twins, ε-twins and their intersections, which act as sources of work hardening. This study provides new insights into deformation behavior of ASSs under cryogenic conditions.

1. Introduction

Austenitic stainless steels (ASSs) have found widespread industrial applications due to their remarkable mechanical and corrosion-resistant properties [1–6]. Among them, SUS316L stainless steel have been paid much attention as a corrosion resistant steel [7,8]. This alloy also exhibits good mechanical properties due to so-called Twinning-Induced Plasticity (TWIP) effect [9–11]. TWIP effect induces significant work hardening, thereby protecting against necking. The activation of twinning during plastic deformation allows for the accommodation of substantial strains without premature necking or failure [9,11,12]. Recently, various high-strength steels, categorized as first to third-generation advanced high-strength steels, have been developed [13,14]. Among them, TWIP steels, including 316L stainless steel, offer the advantage of superior ductility [11,15].

Ensuring the safe and cost-effective storage and transportation of cryogenic fuels are pivotal considerations for the successful integration of these energy sources into a carbon-neutral society. Over the past few years, there has been a notable rise in the use of 316L stainless steel for cryogenic fuel storage and transportation applications, owing to its excellent strength-ductility synergy, adequate toughness, and good corrosion resistance at low temperatures [16–22]. The mechanical characteristics of austenitic 316L steels are predominantly governed by the stability of the metastable austenite phase (γ-fcc), which undergoes martensitic transformations ($\gamma \rightarrow \varepsilon/\alpha'$; $\gamma \rightarrow \varepsilon$ (hcp) $\rightarrow \alpha'$ (bcc)) and mechanical twinning when subjected to plastic deformation or low temperatures [10,11,16,23–30]. This deformation induced martensitic transformations significantly affects the strain hardening response and improve the mechanical properties at cryogenic temperatures [17,31,32]. Further, the influence of low temperature on strain hardening behavior is closely related to the kinetics and nature of martensitic transformations [17,31].

A notable limitation of ASSs lies in their relatively low yield strength in the annealed states, which hampers their suitability for various technological applications. Recently, several approaches have been proposed to strengthen ASSs without compromising their ductility [33,34]. Among these approaches, the introduction of hierarchical microstructures, such as bimodal, gradient, and harmonic

* Corresponding author.
E-mail addresses: singh.digvijay@nims.go.jp (D. Singh), yoshinaka.fumiyoshi@nims.go.jp (F. Yoshinaka), takamori.susumu@nims.go.jp (S. Takamori), emura.satoshi@nims.go.jp (S. Emura), sawaguchi.takahiro@nims.go.jp (T. Sawaguchi).

https://doi.org/10.1016/j.jmrt.2024.09.074
Received 12 June 2024; Received in revised form 15 August 2024; Accepted 11 September 2024
Available online 12 September 2024

nanograins/nano-twinned structures, has been suggested to mitigate the inverse strength-ductility relationship [34–37]. Yan et al., reported that embedding nano-scale twin bundles through high-strain rate dynamic plastic deformation could effectively overcome the strength-ductility balance issue in 316L stainless steel [38]. Similarly, Li et al., observed superior strength and ductility in 316L stainless steel with a heterogeneous lamella structure compared to its coarse-grained counterpart [39]. Liu et al., employed a one-step thermal mechanical treatment-based dislocation strengthening approach without compromising ductility in metastable ASS [40]. However, most of these efforts have focused on optimizing microstructures through severe plastic deformation and thermomechanical processes to achieve a favourable strength-ductility balance at ambient and elevated temperatures.

The strain hardening response of various austenitic stainless steels is primarily governed by the formation of diverse internal microstructures during different stages of plastic deformation. Among the various experimentally observed mechanisms, dislocation glide, deformation twinning, and martensitic transformation are the most established contributors to strain hardening in ASSs at cryogenic temperatures [16,41]. However, there remains significant uncertainty regarding the effects and extent of martensitic transformation mechanisms (e.g., $\gamma \rightarrow \varepsilon \rightarrow \alpha'$, $\gamma \rightarrow \alpha'$) on the strain hardening rate and their overall impact on the strength-ductility balance in ASSs. In a recent study, Li et al. found that deformation-induced α′-martensite played a significant role in increasing strength at temperatures below 173 K, whereas deformation twinning was the primary factor enhancing ductility at temperatures above 173 K [16]. Conversely, Datta et al. found that the $\gamma \rightarrow \varepsilon$ transformation was mainly responsible for the softening observed in the stress-strain curves of metastable ASSs at sub-zero ($\geq$223 K) temperatures [42]. Additionally, several experimental studies have highlighted the influence of strain-induced martensite kinetics on the deformation behavior of ASSs at cryogenic temperatures [17,31,43]. Moreover, it has been found that the contribution to flow stress in 316L steel is directly proportional to the amount of α′-martensite formed during uniform plastic deformation [43]. At cryogenic temperatures, 316L steels exhibit a unique mechanical response, defying conventional understanding by showcasing enhanced strength without sacrificing much ductility [16,43]. The superior ductility observed in materials like 316L stainless steel at cryogenic temperatures challenges the conventional stress-strain balance paradigms. Surprisingly, despite its significance, there exists a conspicuous absence of comprehensive presentations elucidating the mechanistic insights on overcoming the strength-ductility trade-off at low temperatures.

In this study, we embark on a systematic re-examination of the tensile properties of 316L austenitic stainless steel across a spectrum of low temperatures, ranging from ambient conditions down to the frigid realms of 77 K. Our aim is to unravel the intricacies of the stress-strain balance exhibited by 316L stainless steel under cryogenic conditions and shed light on the underlying mechanisms driving its exceptional mechanical performance. We observed internal microstructure by means of electron backscatter diffraction analysis to discuss the reason for the excellent stress-strain balance at cryogenic temperature. Special emphasis is placed on the role of two kinds of martensite, i.e., α′-bcc and ε-hcp and their kinetics to the work hardening mechanism.

2. Experimental

A polycrystalline type-316L stainless steel with a composition of Fe–17.33Cr–12.13Ni–2.09Mo–1.01Mn–0.68Si–0.014C (all compositions in wt.%) was used in this study. Cylindrical tensile specimens with a diameter of 6 mm and a gauge length of 30 mm were prepared for this analysis. Crosshead displacement-controlled tensile loading was applied at an initial quasi-static strain rate of $1.4 \times 10^{-3}\ s^{-1}$, after the specimen was held at a constant temperature ranging from 293 K to 77 K for 1 h in an isothermal chamber. Microstructure analysis was performed using the electron backscatter diffraction (EBSD) technique. The surface for EBSD measurement was prepared by polishing with SiC abrasive paper and subsequently buffing with colloidal silica. The samples were then electrochemically polished using a 6 % perchloric acid solution ($HClO_4$ + C_2H_5OH) at a voltage of 30 V and a temperature of −20 °C. EBSD analysis was conducted using a JEOL JSM-7900F field-emission scanning electron microscope at an acceleration voltage of 20 kV and a working distance of 15 mm. EBSD data processing was conducted using TSL-OIM software. A minor cleanup operation was applied to low-confidence index (CI < 0.1) EBSD data. X-ray diffraction (XRD) analysis was conducted using a Rigaku SmartLab equipped with Co-Kα radiation (40 kV, 35 mA, λ = 1.789 Å) on both the pre-deformed and post-deformed specimens to identify the constituent phases at different temperatures.

3. Results

3.1. Tensile properties at low temperatures

In general, when considering chemical composition, an increase in ultimate tensile stress often results in a decrease in elongation, and vice versa. However, TRIP and TWIP steels exhibit exceptional stress-strain balance attributed to work hardening through γ-twinning and formation of α′- and ε-martensite. In our study, particular emphasis is placed on enhancing stress-strain balance solely through temperature reduction. Fig. 1(a) shows the engineering stress-strain curve of the tensile tested specimens at low temperature range of 293 K – 77 K. The 316L stainless steel showed strong temperature dependent tensile properties with inverted s-type stress-strain behaviour at temperatures below 223 K. The tensile properties estimated in the entire cryogenic range of temperatures are listed in Table 1. The ultimate tensile strength (UTS) increases gradually with temperature drop and becomes doubles (1280 MPa) at 77 K. Fig. 1(b) shows 0.2 % proof stress (yield strength, σ_y), UTS vs. total elongation (TE), uniform elongation (UE) as a function of temperatures. Nearly 50 % increase in yield strength is observed at 77 K, which is less than the UTS rise with temperature drop. This could be mainly because of low carbon (0.016 wt.%) in 316L stainless steel which are known to have considerable effect on the yield strength at low temperatures [44,45]. Surprisingly, unlike most of conventional structural materials, the ductility didn't drop gradually with decrease in temperatures. A nominal drop of approximately 12 % – 15 % in total elongation is observed at 77 K compared to room temperature tested specimens. However, the uniform elongation remains almost constant over the entire cryogenic deformation range. It is worth to note here that the maximum TE and UE values are observed at sub-zero temperature of 223 K.

Fig. 1(c) presents a comprehensive overview of the strength-ductility trade-off in various steels at room temperature [40,46]. At ambient temperature, ASS typically demonstrate a strength-ductility balance within the range of 40 GPa%. It is confirmed that UTS increase with decreasing temperature without much decrease in uniform elongation. Notably, an exceptional strength-ductility balance surpassing the 80 GPa% threshold is obtained at 77 K.

3.2. Temperature-dependent strain hardening behavior

In this section, the work hardening behavior, similar to that observed in TRIP and TWIP steels, is analyzed to explore the phenomenon of delayed necking. A clear temperature dependency is evident in the strain hardening response of 316L steel, as shown in Fig. 2(a and b). The strain hardening rate ($d\sigma/d\varepsilon_t$) gradually increases with decreasing temperature across the deformation range. At 223K, the 316L steel exhibits a constant $d\sigma/d\varepsilon_t$ of approximately 2 GPa over a larger strain region compared to specimens deformed at ambient temperature. This expanded strain-hardening region likely contributes to the observed increase in elongation at 223 K. However, below 223 K, a transition from single-stage to two-stage hardening behavior occurs. Unlike at RT, after

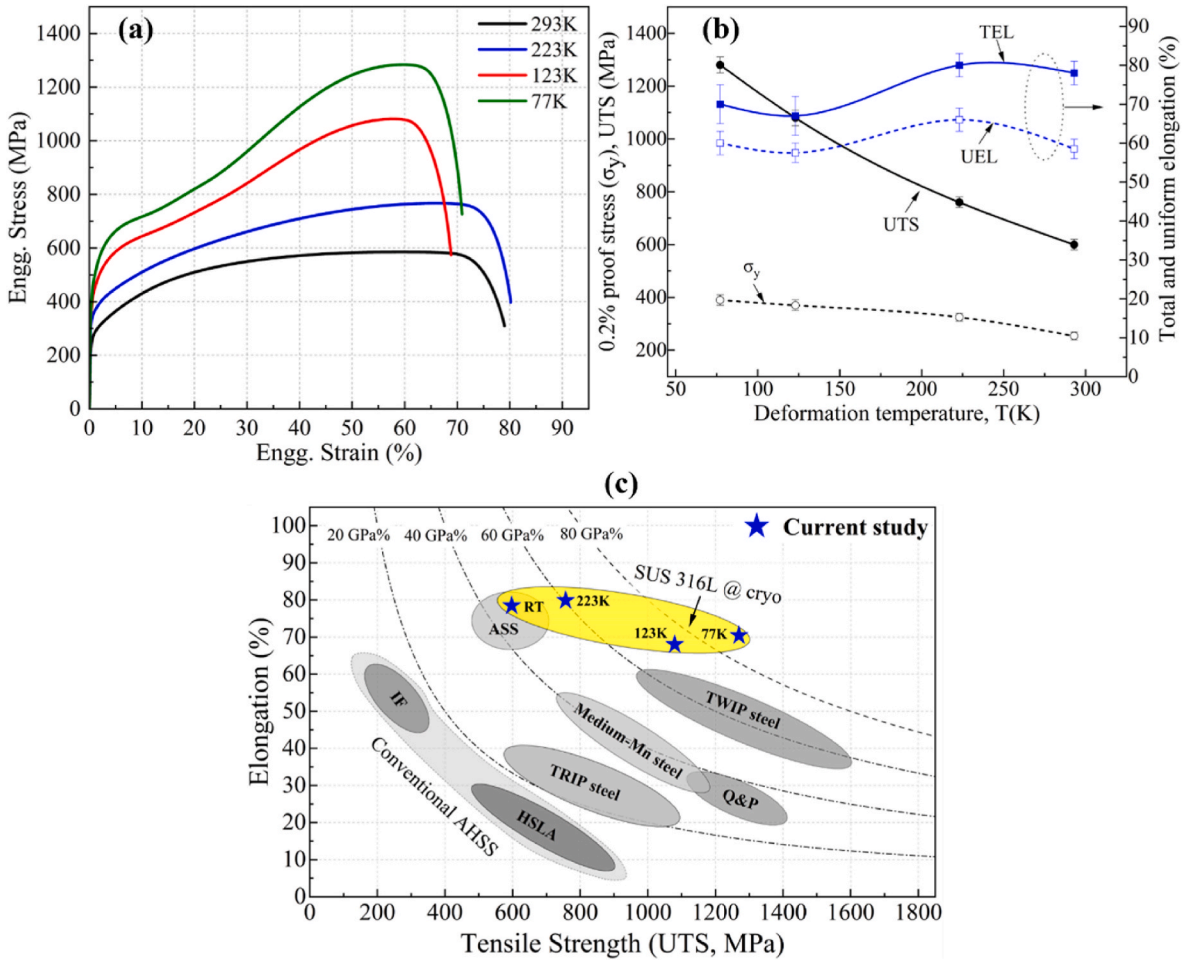

Fig. 1. *(a) Engineering stress-strain curves of the tensile deformed specimens at cryogenic temperatures. (b) 0.2 % proof stress, UTS vs. Total elongation (TEL), uniform elongation (UEL) variation at different cryogenic temperatures. (c) strength-ductility trade-off in various steels* [40,46].

Table 1
Tensile properties of 316L austenitic stainless steel at various low temperatures.

Temperature (K)	0.2% proof strength (MPa)	Tensile strength (MPa)	Uniform elongation UE (%)	Total elongation TE (%)
293 (RT)	254	600	58.5	78
223	325	760	66	80
123	370	1080	57.5	67
77	390	1280	60	70

a rapid drop in $d\sigma/d\varepsilon_t$ value during the initial stage, a steep increase in the strain hardening rate is observed during the secondary hardening stage. Furthermore, two distinct hardening characteristics (regions I & II) are evident in the secondary hardening regime, as illustrated in Fig. 2 (b). During the initial deformation (true strain, $\varepsilon_t = 0.1 - 0.2$), the strain hardening rate gradually increases in region II. In contrast, in region III ($\varepsilon_t > 0.2$), a steep increment in the $d\sigma/d\varepsilon_t$ is observed. The unique nature of this secondary hardening stage at temperatures of 123 K and 77 K could be attributed to the diverse deformation mechanisms operating in 316L steel under cryogenic conditions. Additionally, maximum $d\sigma/d\varepsilon$ values of approximately 3.5 GPa and 4.5 GPa are estimated at temperatures of 123 K and 77 K, respectively. Importantly, the true strain value (ε_t) at which $d\sigma/d\varepsilon$ reaches its global maximum decreases with decreasing temperature.

The Considère criterion for plastic instability is a critical factor in determining the onset of necking in the stress-strain curve of ductile materials [47]. Necking occurs when the stress-strain response satisfies the plastic instability conditions, expressed as:

$$d\sigma / d\varepsilon_t \leq \sigma \quad (1)$$

Since, the strengthening effect of strain hardening is insufficient to counterbalance the stress loss caused by the decreasing cross-sectional area. The stress-strain curves obtained at low temperatures adhere to the Considère criterion, as illustrated in Fig. 1(a and b). Plastic instability stress (PIS), representing the true stress values at which the Considère criterion is satisfied, is plotted in Fig. 2(c) alongside the true uniform elongation (ε_{ut}) for various low temperatures. At these reduced temperatures, the ε_{ut} value remains relatively stable within the range of 0.45 – 0.5, while the PIS experiences a significant increase, nearly doubling to 2 GPa at 77 K. Consequently, the plastic instability conditions are met at relatively large strains, leading to enhanced uniform elongation at low temperatures.

3.3. Deformed microstructure: EBSD analysis

Fig. 3 presents an overview of EBSD microstructural analysis conducted on tensile-fractured specimens at different temperatures. This analysis includes colored phase maps and their corresponding inverse pole figure (IPF) maps, captured at both low and high magnifications. Following tensile fracturing at room temperature (293 K), the microstructure predominantly consists of austenite (γ-fcc), with no discernible presence of martensitic phases, as depicted in the phase map in Fig. 3(a). However, the corresponding IPF map reveals a significant degree of twinning within the (111) oriented grains, evidenced by the pronounced

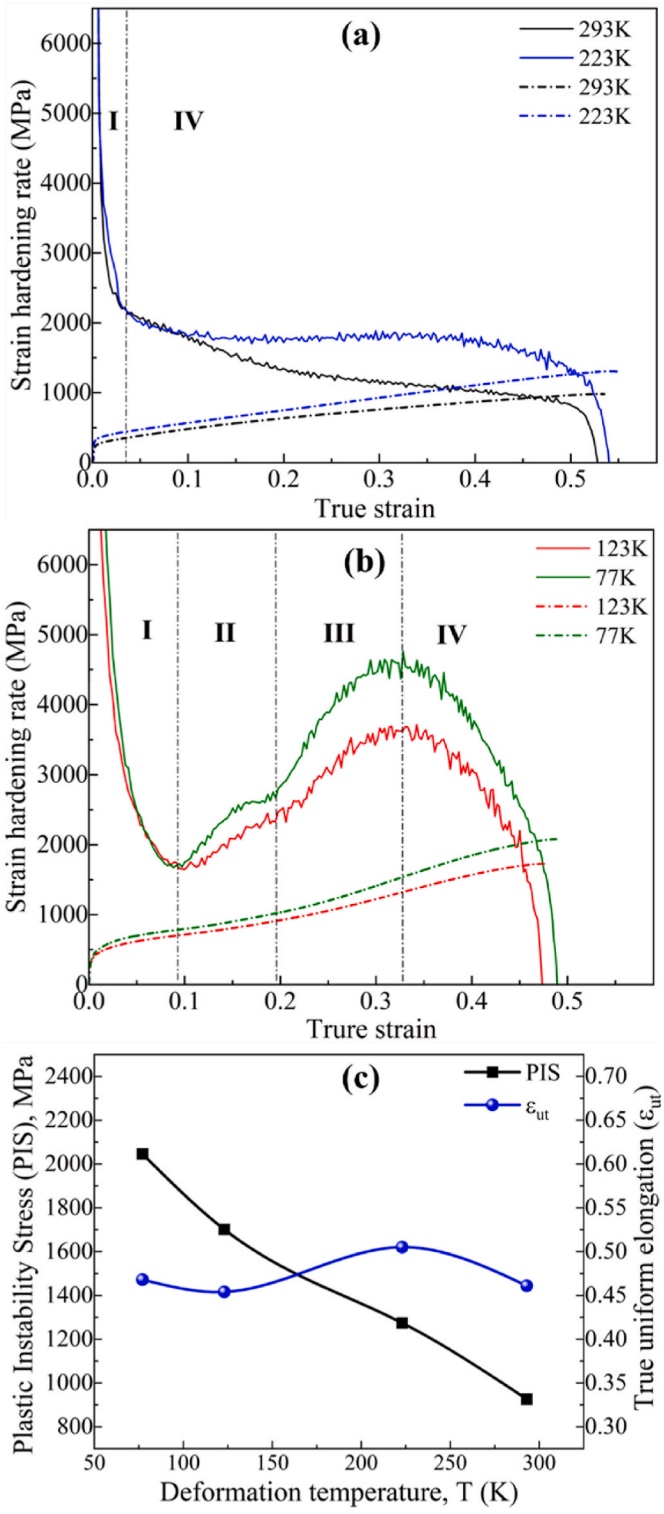

Fig. 2. *(a, b) Strain-hardening rate/true stress vs. true strain curves of the tensile deformed specimens at different cryogenic temperatures (77 K – 293 K). (c) Plastic instability stress (true stress) and true uniform strain (ε_{ut}) vs temperature curve in the necking region (at Considère criteria).*

color gradient in Fig. 3(b). Furthermore, the high-magnification IPF map presented in Figs. 3(b-1) confirms the occurrence of Σ3-type deformation twinning (γ-twin) with a 60° misorientation. Upon subjecting the specimens to a deformation temperature of 223 K, a noticeable presence of ε-martensite phase (approximately 5 – 8 %) is detected in the phase map of the tensile-fractured specimen, alongside γ-twinning, as illustrated in Fig. 3(c and d). Additionally, the enlarged γ-IPF map reveals that ε-martensite tends to nucleate and grow preferentially at austenite grain boundaries and γ/γ-twin interfaces within (111) oriented grains. The low confidence index (CI) value observed in the ε-martensite rich region may be attributed to its extremely fine size and severe straining during the γ → ε transformation.

Unlike at RT and 223 K, the tensile-fractured specimen at 123 K exhibits a triple-phase microstructure comprising γ-fcc, ε-hcp, and α′-bcc martensite phases, as illustrated in Fig. 3(e and f). The estimated amounts of ε- and α′-martensite are approximately 15 % and 35 %, respectively. Alongside the martensite phases (ε and α′), γ-twinning is also observed at 123 K, as evidenced by the enlarged γ-IPF map in Figs. 3 (f-1). Moreover, the enlarged α-IPF map depicted in Fig. 3(f-3) reveals a diverse array of colors, indicating that the deformation-induced martensite exhibits various crystallographic orientations. The presence of these multiple variants of α′-martensite can be attributed to the activation of different slip systems within {111} planes during deformation. At 77 K, a γ/ε/α′ triple-phase microstructure analogous to that observed at 123 K is generated in the tensile-fractured 316L steel specimen, as depicted in Fig. 3(g and h). However, the amount of α′-martensite phase significantly increased in the microstructure with a temperature drop to 77 K. The enlarged γ-IPF map presented in Figs. 3(l-1) reveals the presence of very fine parallel γ-twins along the γ/α′ interfaces.

3.4. Microstructure evolution: effect of cryo-temperature

To explore the microstructural evolution and deformation mechanisms at cryogenic temperatures, the tensile test was interrupted at an intermediate strain level of 20 % (referred to as T-20), in addition to the point of fracture (TF). The subsequent sections provide a detailed XRD and EBSD examination of the influence of deformation level on the microstructural evolution of 316L steel at various low temperatures.

Fig. 4 shows the XRD patterns of the undeformed, T-20, and TF specimens, as well as the relationship between martensite phase fractions (ε-hcp, α′-bcc) and engineering strain during tensile deformation at various low temperatures. The volume fractions of the ε-martensite and α′-martensite phases in the microstructure were calculated from the XRD profiles using the reference intensity ratio (RIR) method with PDXL (Rigaku) software [48]. The as-received (AR) specimens exhibited a fully austenitic spectrum. After 20 % deformation, peaks corresponding to ε- and α′-martensite phases emerged in the diffraction pattern below 223 K, as shown in Fig. 4(a). In the tensile-fractured specimens, the $(110)_{\alpha'}$ peak intensity gradually increased at the expense of γ- and ε-phase peaks with decreasing temperature, as shown in Fig. 4(c). This impact is evident in the estimated phase fractions shown in Fig. 4(b–d). Initially, the amount of ε-martensite increases with decreasing temperature but then drops with further deformation. In the T-20 deformed pattern, approximately 14 % and 21 % ε-martensite are estimated at 123 K and 77 K, respectively. After tensile fractured (TF), the estimated amount of ε-martensite drops to 12 % and 6 % at 123 K and 77 K, respectively. Conversely, the amount of α′-martensite gradually increases with lower temperatures, reaching approximately 78 % volume fraction in the TF microstructure at 77 K.

3.4.1. At 223 K

Fig. 5 illustrates the EBSD microstructure findings of specimens deformed to 20 % strain and fractured strain at 223 K. At 20 % strain, Σ3 γ-twin is predominantly observed in the deformed microstructure, as highlighted in the phase map and corresponding IPF map in Fig. 5(a–c). No deformation-induced martensitic transformation (ε or α′) is evident at this stage of deformation. However, ε-martensite phase (depicted in green) is detected in the microstructure of the post-fractured specimen, alongside the presence of γ-twinning, as shown in the phase map in Fig. 5(b) ε-martensite tends to form along γ-fcc grain boundaries and γ/γ-twin interfaces within the (111) oriented grains. Additionally,

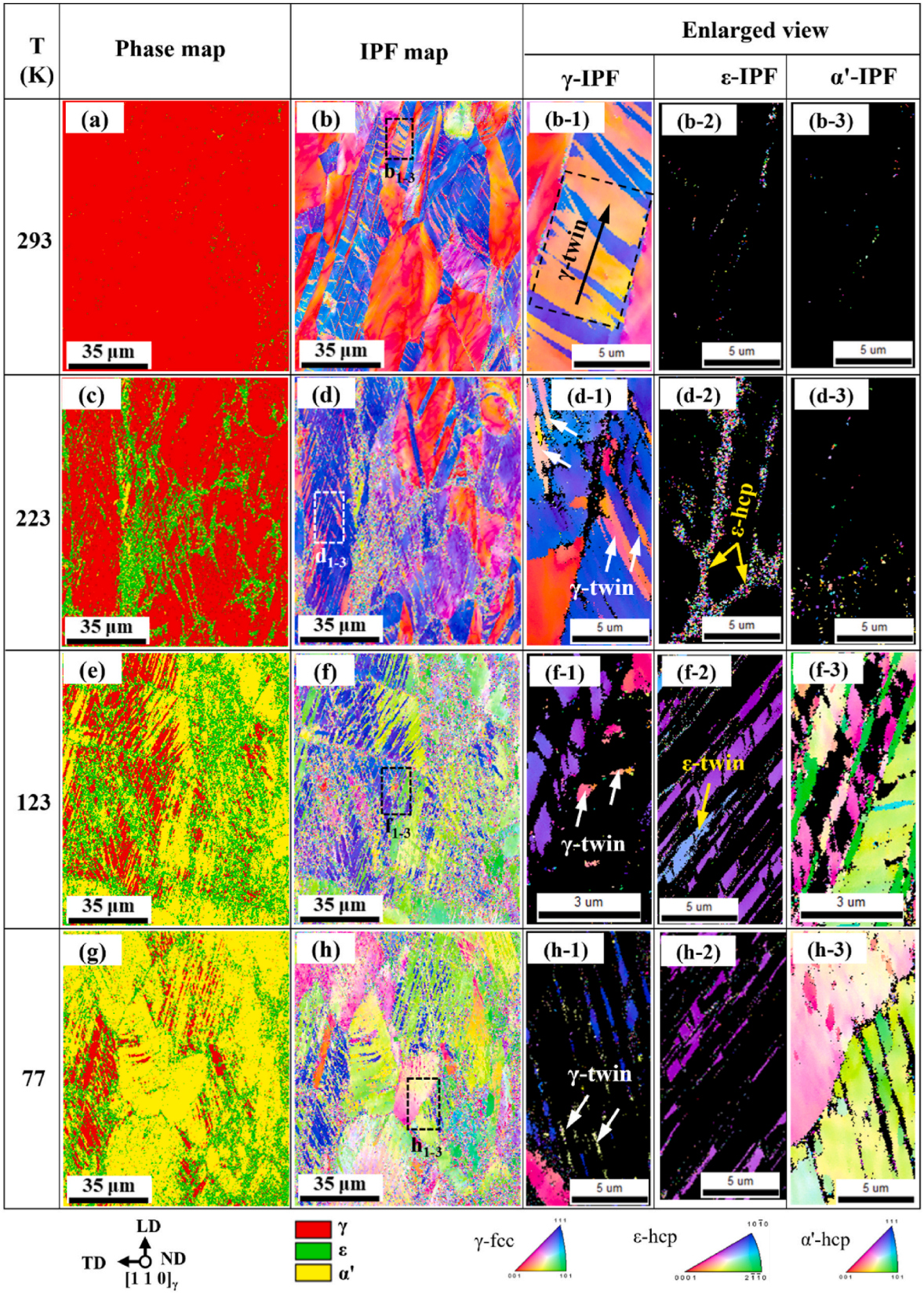

Fig. 3. *A detailed overview of EBSD phase map and inverse pole figure (IPF) maps of tensile fractured (TF) 316L steel specimens at various low temperatures (293 K – 77 K).*

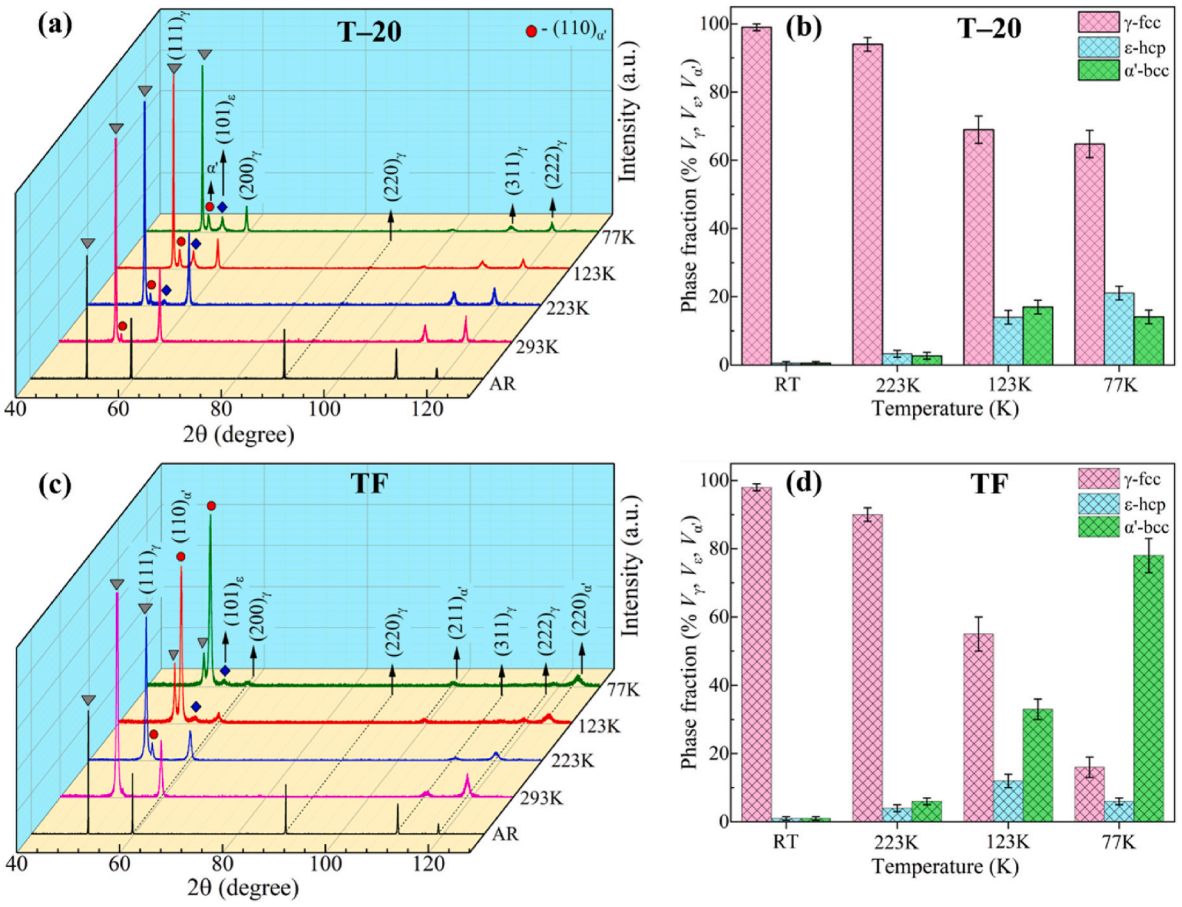

Fig. 4. *(a, b) XRD patterns and corresponding martensite phase fractions evolved in the 20 % strained (T-20), and (c, d) tensile fractured (TF) specimens at various low temperatures (293 K – 77 K).*

γ-twin density increases in the deformed microstructure with the plastic strain.

3.4.2. At 123 K

Fig. 6 presents the EBSD microstructure findings of 20 % strained and post-fractured specimens at 123 K. At the 20 % strain, the deformed microstructure exhibited triple-phase structures (γ/ε/α′), as depicted in the phase map in Fig. 6(b). Most of the α′-martensite and deformation twins (Σ3-type) are generated within <111> oriented grains, as shown in IQ and IPF maps in Fig. 6(a–c). However, the parent γ-austenite phase predominates within the microstructure at this early stage of deformation. Fig. 6(d–g) illustrates the high-magnification phase and IPF maps of the deformed γ-fcc grains oriented nearly along the <212> direction, as highlighted in the IQ map in Fig. 6(a). The corresponding ε-IPF map revealed the occurrence of single variant ε-martensite parallel bands along the primary operational shear with the highest Schmid factor (~0.47), as shown in Fig. 6(f). However, two distinct α-martensite variants (α'_1 and α'_2) with different orientation and morphology are observed in 20 % strained microstructure, as seen in Fig. 6(g) α'_1-martensite is associated with the two-step γ → ε → α′ transformation mechanism, where it nucleates and grows inside the intermediate ε-martensite phase. Meanwhile, α'_2-martensite plates form parallelly along the ε-hcp bands as a result of direct γ → α′ transformation. Additionally, the corresponding pole figures (Fig. 6(h)) establish the following crystallographic orientation relationships among the γ-ε-α′ phases:

$$\text{Shoji–Nishiyama (S-N)}: (1\,1\,1)_{\gamma}\,//\,(0\,0\,0\,1)_{\varepsilon}, <1\,0\,\bar{1}>_{\gamma}\,//\,<2\,\bar{1}\,\bar{1}\,0>_{\varepsilon}.$$

$$\text{Kurdjumov-Sachs (K-S)}: (1\,1\,1)_{\gamma}\,//\,(1\,0\,1)_{\alpha 1}, <1\,0\,\bar{1}>_{\gamma}\,//\,[1\,1\,\bar{1}]_{\alpha 1}$$

$$\text{Nishiyama–Wassermann (N-W)}: (1\,1\,\bar{1})_{\gamma}\,//\,(0\,1\,1)_{\alpha 2}, <1\bar{1}0>_{\gamma}\,//\,<001>_{\alpha 2}$$

As plastic strain progresses towards fracture (TF), a notable increase in the predominance of γ → α′ transformation is observed, leading to a significant rise in the lenticular α′-martensite fraction within the microstructure. Meanwhile, the fraction of ε-martensite experiences a marginal decrease, as illustrated in the phase map in Fig. 6(i). Moreover, a significant reduction in the size of α′-martensite laths is observed with the progression of plastic deformation at 123 K, as depicted in high-magnification phase and IPF maps in Fig. 6(j and k). The α′-IPF map depicted in Fig. 6(k) reveals the intricate structure of lath martensite. Here, the parent austenite matrix undergoes transformation into martensite packets with the same habit plane, as highlighted in pink (packet boundary, PB). Each packet is further subdivided into group

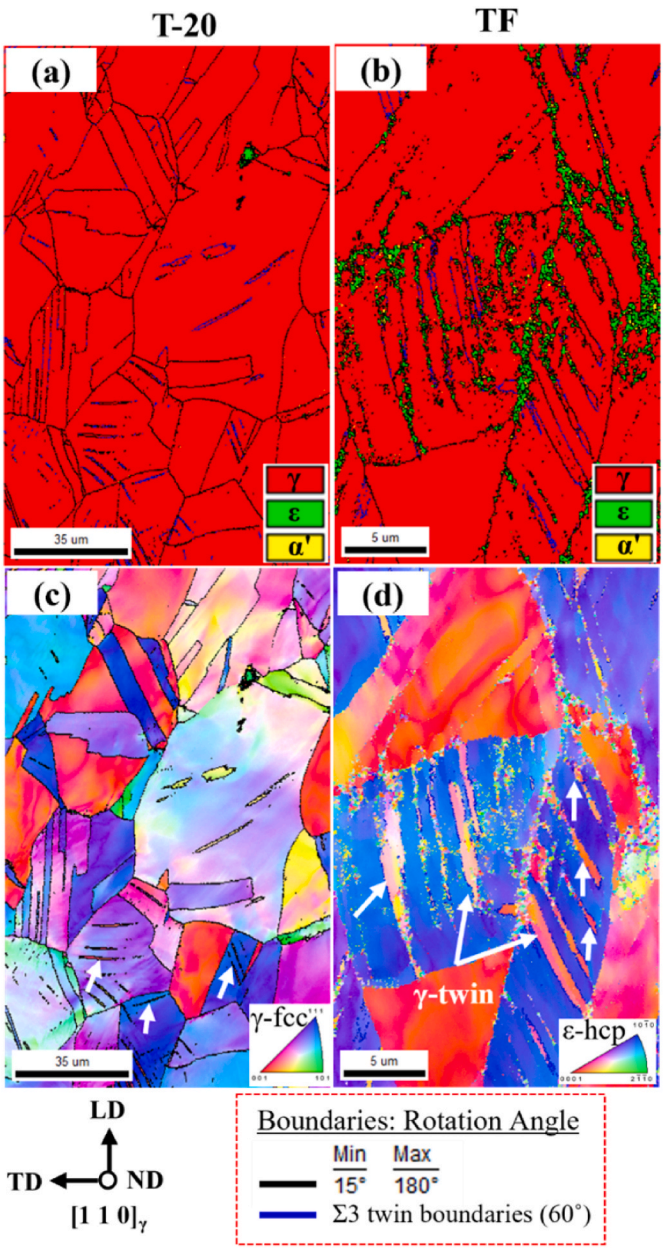

Fig. 5. (a, b) EBSD phase maps and (c, d) inverse pole figure (IPF) maps of 20 % strained (T-20) and tensile fractured (TF) specimens at 223 K. White arrows in the IPF maps indicate the Σ3-type twin boundaries in the γ-austenite phase.

boundaries containing several laths, as indicated in black in Fig. 6(j). These α′-martensite variants are closely associated with the packet boundaries (PBs) of the parent γ-phase, as highlighted in pink in the phase map (Fig. 6(f)).

3.4.3. At 77 K

The EBSD microstructure of the specimen deformed to 20 % strain (T-20) and subsequently fractured at 77 K is depicted in Fig. 7. Similar to the results at 123 K, the deformed microstructure exhibited triple-phase structures (γ/ε/α′) at 20 % strain, as shown in Fig. 7(a–c). The phase map and corresponding IPF maps shown in Fig. 7(d–g) represent high-magnification EBSD results obtained from the highlighted region in Fig. 7(a), where austenite grains are predominantly oriented along the <101> direction. Alongside the conventional γ/ε/α′ triple-phase microstructure, γ-twins and (1 0 $\bar{1}$ 2) type ε-twins are generated, as evidenced by the IPF maps in Fig. 7(e and f). Similar to the observations at 123 K, fine-sized α′-martensite laths with different crystal orientations are generated in the T-20 specimens at 77 K. These multiple α-martensite variants are associated with a maximum of 24 K–S variants plausible in the γ-fcc matrix. Interestingly, α′-martensite formed inside γ-twin during one-step ($\gamma/\gamma_{twin} \rightarrow \alpha'$) transformation exhibits larger lath sizes than those formed during two-step transformations, as shown in Fig. 7(g). Pole figure analysis establishes the S – N and K – S ORs among γ/ε and γ/α′ interfaces, respectively, as depicted in Fig. 7(h).

Upon reaching the onset of fractured strain (TF), a notable increase in the $\gamma \rightarrow \alpha'$ transformation is observed, resulting in a significant rise in the α-bcc phase (~80 %) and a substantial decrease in ε-martensite content within the microstructure at 77 K, as shown in the phase map in Fig. 7(f). Meanwhile, the average lath size of the α′-martensite phase is estimated to be 0.24 μm, based on the high-magnification phase map presented in Fig. 7(j). The strength and toughness imparted by deformation-induced α′-martensite on metastable austenitic stainless steel are strongly influenced by the size of the packets and blocks. Therefore, understanding the morphology of α′-martensite is of paramount importance.

4. Discussion

The anomalous strength-ductility balance observed at cryogenic temperatures stems from the slow martensitic transformation, resulting in the maximum strain-hardening rate occurring at the onset of necking where plastic instability criteria were met. The strength-elongation balance of the specimen was highest at 77 K and lowest at 293 K, as indicated by the nominal stress-strain curves. Based upon the experimental observations, the invocation of the conventional strength-ductility trade-off of 316L ASS at cryogenic temperatures could be linked to following factors: (i) delayed plastic instability criteria, (ii) slow deformation induced martensitic transformation kinetic, and (iii) Change in plasticity mechanism from deformation twinning to martensitic transformation ($\gamma \rightarrow \varepsilon \rightarrow \alpha'$) below 223K. This change is influenced by the stacking fault energy (SFE) and Gibbs free energy variations with temperature, resulting in the generation of a hierarchical microstructure during deformation. The effects of these factors on the strain-hardening behavior and strength-ductility synergy of the 316L ASS at cryogenic temperatures are discussed in this section.

Three plasticity modes were mainly operated during cryogenic tensile deformation: deformation twinning, ε-martensitic, and α-martensite transformation. The characteristic plasticity mode contributing to the work hardening rates changed with the deformation temperature and plastic strain. The influence of low temperature on the plasticity mechanism of 316L ASS was evident through EBSD findings, where a decrease in temperature to sub-zero levels induced the transition from deformation twinning to martensitic transformation. Consequently, a two-stage hardening associated with martensitic ($\gamma \rightarrow \varepsilon \rightarrow \alpha'$) induced TRIP effect was reflected in the nominal stress-strain and strain-hardening rate curves at deformation temperatures below 223 K, as shown in Figs. 1 and 2. Furthermore, not only the deformation temperature but also the degree of plastic strain notably influenced the plasticity mechanisms. At 223 K, deformation twinning was the primary governing deformation mechanism observed in the 316L ASS. However, the noticeable presence of ε-martensite was also observed during the later stage of deformation. The combined occurrence of TWIP and ε-TRIP effects resulted in a more sustainable and moderate strain hardening rate to a larger plastic strain, hence resulting in the highest ductility exerted at 223 K. Similarly, the effect of plastic strain could be observed at 123 K and 77 K, where the dominating plasticity mechanism changed from a $\gamma \rightarrow \varepsilon$ to $\gamma/\varepsilon \rightarrow \alpha'$ martensitic transformation with an increase in plastic deformation.

It is worth mentioning that these individual plasticity mechanisms have distinct contributions to the strain hardening behavior of 316L ASS. Among the three different deformation modes, deformation

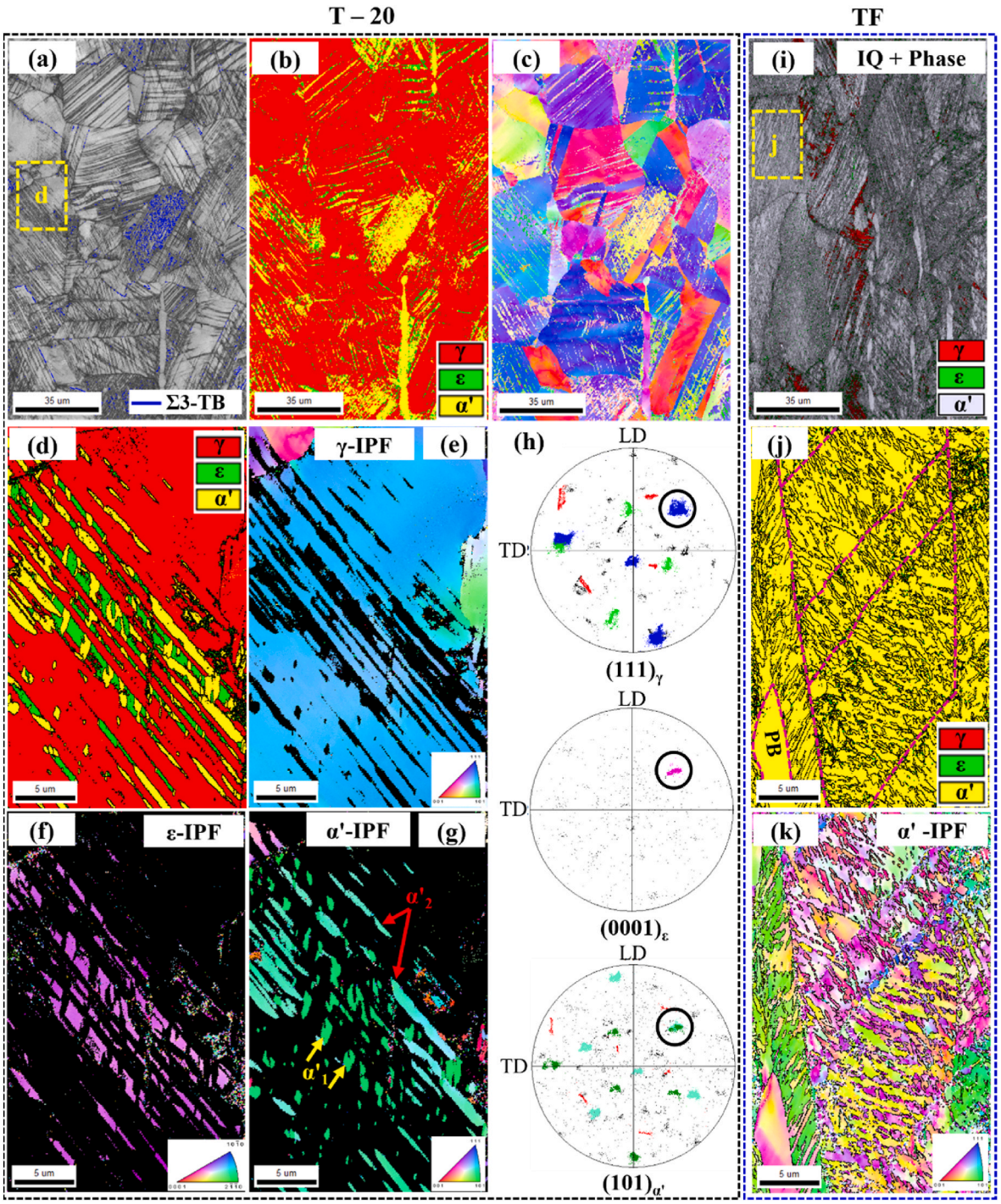

Fig. 6. *(a-c) Low-magnification IQ map, phase map, and IPF map of the 20 % strained (T-20) specimen at 123 K. (d-g) High-magnification phase map and corresponding γ-, ε-, and α′-IPF maps of the highlighted <212> grain in (a). (h) Pole figures for (1 1 1)$_\gamma$, (0 0 0 1)$_\varepsilon$, and (1 0 1)$_{\alpha'}$ corresponding to the γ-, ε-, and α′-regions shown in (e-g). (i-k) Low- and high-magnification EBSD phase maps and corresponding IPF map of the tensile fractured (TF) specimen at 123 K. In (i), α′-martensite is marked by white colour.*

twinning exerted the lowest strain hardening rate of around 2 GPa, as shown in Fig. 2 (b). Below 223 K, two distinct slopes are observed within the secondary hardening stage (regions II and III) of the $d\sigma/d\varepsilon_t$ vs true strain plots. In region II (ε_t = 0.1 – 0.2), the $d\sigma/d\varepsilon$ value increases gradually and attains its maximum of 2.5 GPa, corresponding to predominantly γ → ε transformation and γ-twinning. Whereas in region III ($\varepsilon_t > 0.2$), a steep increase in the $d\sigma/d\varepsilon_t$ slope is observed associated with direct γ/ε → α′ martensitic transformation at cryogenic temperatures (123 K and 77 K). The occurrence of a large amount of α′-martensite during the later stage of deformation has resulted in the highest $d\sigma/d\varepsilon_t$ value of around 4.5 GPa at 77 K. The Considère criterion for plastic instability has been satisfied for all the cryogenic tested conditions. Even though the plastic instability stresses decreased with increases in the deformation temperature, the true uniform strain remained constant or increased noticeably throughout the cryogenic temperatures. Therefore, meeting the PIC condition at a later stage of deformation, i.e., high ε_{ut}, is primarily responsible for delaying necking and enabling a large uniform elongation at cryogenic temperatures. The differences in strain hardening behaviour between specimens deformed at 123 K and 77 K, such as the variation in the maximum $d\sigma/d\varepsilon_t$ value (3.5 GPa and 4.5 GPa,

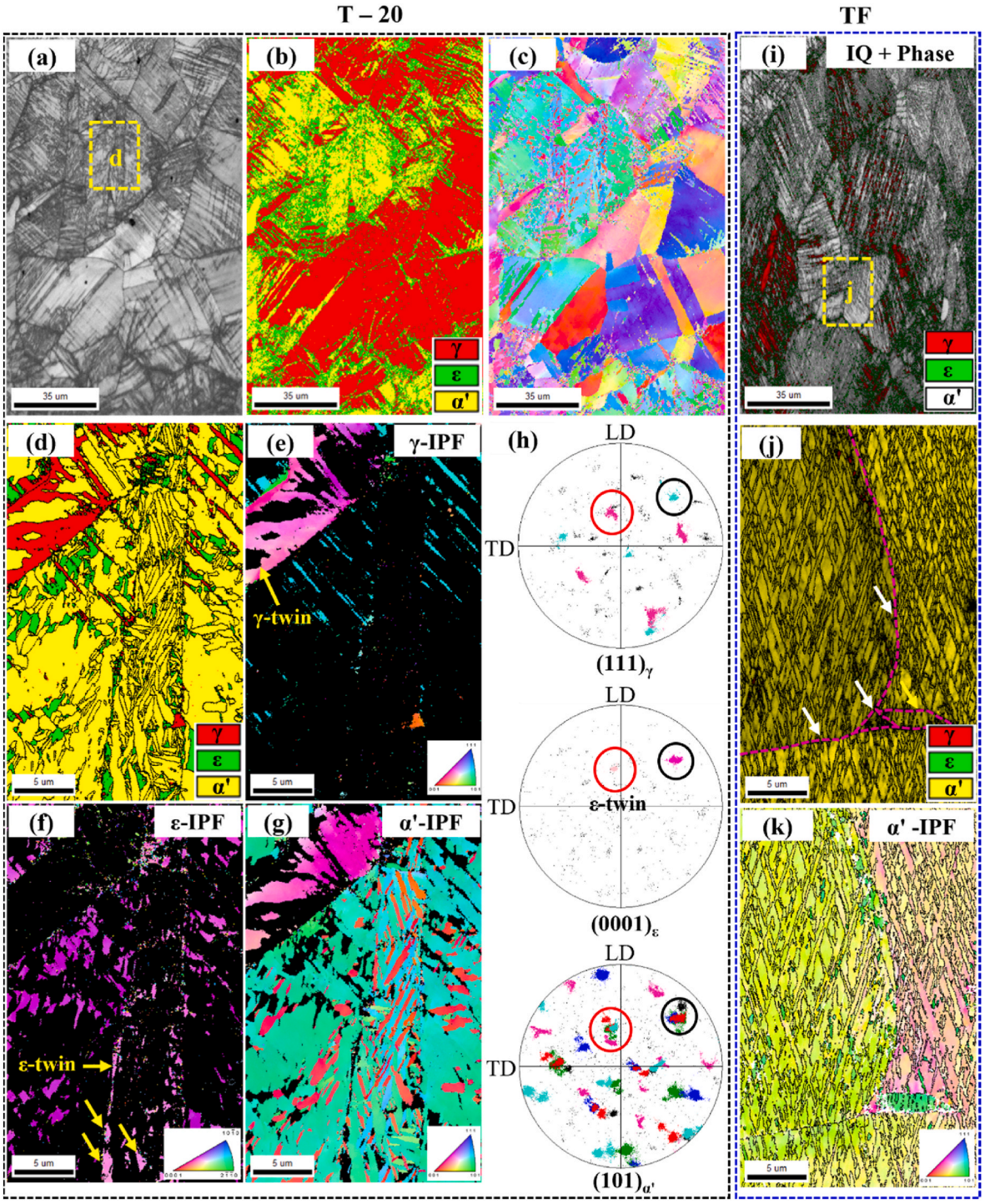

Fig. 7. *(a-c) Low-magnification IQ map, phase map, and IPF map of the 20 % strained (T-20) specimen at 77 K, respectively. (d-g) High-magnification phase map and corresponding γ-, ε-, and α′-IPF maps of the highlighted <101> grain in (a). (h) (1 1 1)$_γ$, (0 0 0 1)$_ε$, and (1 0 1)$_{α'}$ pole figures corresponding to the γ-, ε-, and α′-phase shown in (e-g). (i-k) Low- and high-magnification EBSD phase maps and the associated IPF map of the tensile fractured (TF) specimen at 77 K. In (i), α′-martensite is marked by white colour, and white arrows in (k) indicate the pocket boundaries associated with different variants of α′-martensite.*

respectively) and the plastic strain values corresponding to the onset of region III, primarily stem from the alteration in thermodynamic stability (Gibbs free energy, ΔG) among γ-, ε-, and α′-phase. This change in phase stability consequently affects the kinetics of martensitic transformation at these cryogenic temperatures.

Stacking fault energy (Γ_{SFE}) and phase stability (Gibbs free energy, $\Delta G^{\gamma \rightarrow \varepsilon}$) are crucial factors to govern various martensitic transformations (γ → ε, γ → ε → α′ or reversible γ ↔ ε) and deformation twinning mechanism in metastable austenitic steels [16,49–51]. Therefore, studying the role of $\Gamma_{SFE}/\Delta G^{\gamma \rightarrow \varepsilon}$ is crucial to understand the complex interaction between microstructure evolution, deformation mechanism, and tensile behavior of austenitic stainless steel at cryogenic temperatures. It is established that depending on the SFE value, distinct plasticity mechanism such as martensitic transformation ($\Gamma_{SFE} <$ 18 mJ/m^2), deformation twinning (18 mJ/m^2 < Γ_{SFE} < 45 mJ/m^2), and dislocation slip ($\Gamma_{SFE} >$ 18 mJ/m^2) can be activated in austenitic steels

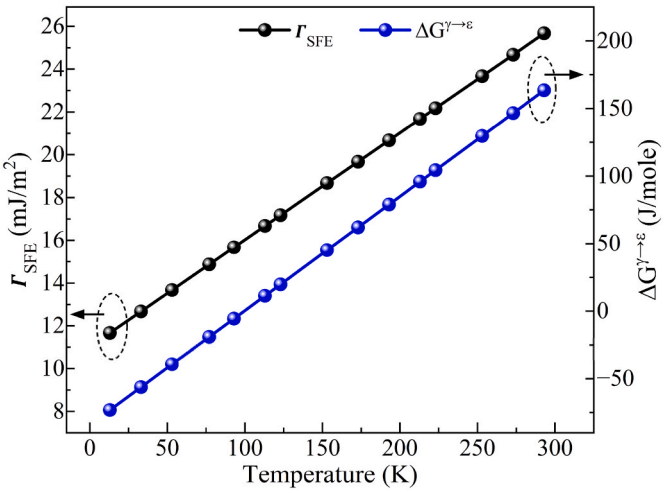

Fig. 8. *Variation in Gibbs free energy ($\Delta G^{\gamma\to\varepsilon}$) and stacking fault energy (Γ_{SFE}) of SUS 316L steel with deformation temperatures.*

[16,52,53]. Fig. 8 illustrates the variation in Gibbs free energy and SFE of 316L ASS at various cryogenic temperatures. For a given deformation condition, SFE can be expressed by Olson and Cohen equation [54]:

$$\Gamma_{SFE} = 2\rho\Delta G^{\gamma\to\varepsilon} + 2\sigma \tag{2}$$

where ρ (2.959 x 10^{-5}) is molar surface density and σ represents the interfacial energy for the γ/ε interface, considered as 8 mJ/m^2 throughout the low temperature, which is a typical value assumed for similar alloy compositions [55]. Additionally, T. Yonezawa et al., analytical methods based on chemical compositions are employed for SFE calculation at ambient temperature (T_0), as presented in equation (3) [56].

$$\text{SFE}\left(\Gamma_{SFE(T0)}, \text{mJ}/\text{m}^2\right) = -7.1 + 2.8\text{Ni} + 0.49\text{Cr} + 2\text{Mo} - 2\text{Si} + 0.75\text{Mn} - 5.7\text{C} - 24\text{N} \tag{3}$$

Furthermore, the temperature effect on SFE of 316L ASS is considered using the established relationship [57]:

$$\Gamma_{SFE\ (T)} = \Gamma_{SFE\ (T0)} + 0.05\ (T - 293) \tag{4}$$

At ambient temperature (293 K), the $\Gamma_{SFE\ (T0)}$ and $\Delta G\gamma\to\varepsilon$ values of 316L steel used in this study are estimated approximately as 25 mJ/m^2 and 160 J/mol, respectively. This accounts for observing deformation twinning as the sole plasticity mode at room temperature. At 223 K, the SFE value drops to around 20 mJ/m^2, leading to deformation prevailed by γ-twinning. During later stages of deformation, additional mechanical driving force resulted in the occurrence of ε-martensite as a secondary plasticity mode. This facilitated extra strain hardening and uniform elongation observed at 223 K. With further temperature decrease to 77 K, the SFE values fall well below 18 mJ/m^2 ($\Gamma_{SFE,\ 77K}$ = 12 mJ/m^2), making martensitic transformation ($\gamma \to \varepsilon \to \alpha'$) the primary deformation mechanism operative at such low temperatures. Moreover, the stability of the γ-phase also significantly decreases below 123 K ($\Delta G^{\gamma\to\varepsilon} \leq 0$), leading to the dominance of martensitic phases in the tensile-deformed microstructures at 123 K and 77 K. Although 316L ASS exhibits similar qualitative deformation characteristics at 123 K and 77 K, the quantitative differences in strain hardening rate and tensile properties can be attributed to the thermodynamic phase stability differences between these two temperatures. The notable reduction in SFE and $\Delta G^{\gamma\to\varepsilon}$ results in an increase in martensitic transformation kinetics at 77 K compared to 123 K.

The superior strength-ductility balance of 316L steel at cryogenic temperatures are attributed to the sustained high strain hardening rates. Martensite transformation kinetics played a significant role in maintaining this sustainable strain-hardening rate during the later stages of plastic deformation at cryogenic temperatures. At 223 K, both XRD and EBSD analyses unveil markedly sluggish martensite kinetics, accompanied by a minimal fraction of both ε- and α′-phases (see Fig. 4). However, as the deformation temperature decreased below 223 K, we observed a sharp increase in ε-martensite kinetics during the initial stage of deformation, while α′-martensite transformed slowly. As plastic strain increased, the amount of α′-martensite increased at the expense of ε-martensite and γ-austenite at 123 K and 77 K. This increase in α′-martensite phase fraction in the microstructure is associated with the transformation of less stable ε-martensite into more stable α′-martensite during the two-stage $\gamma \to \varepsilon \to \alpha'$ transformation.

From the cryogenic strain-hardening behavior of 316L stainless steel, it is evident that α-martensite contributes the most to enhancing the strain hardening rate (~4.5 GPa) among the three different structures generated (γ-twinning, ε-, α'-) during deformation. Koyama et al. reported similar findings concerning Fe–Mn–C TWIP steels, wherein the increase in the work hardening rate with deformation modes was ranked as follows: ε-martensitic transformation, deformation twinning, and dynamic strain aging [47]. Therefore, it is not only the maximum $d\sigma/d\varepsilon_t$ value that matters, but also the degree of deformation, i.e., plastic strain, at which it reaches its global maximum, that is crucial for achieving the superior strength-ductility balance of a material. Hence, the sluggish α′-martensite kinetics during the initial stage of deformation has played a vital role in achieving the global maximum of $d\sigma/d\varepsilon_t$ close to the fracture strain. As a result, the meeting of the PIC criteria is delayed, consequently allowing 316L stainless steel to exhibit a very large uniform elongation at cryogenic temperatures.

Besides the kinetics of martensitic transformation, the formation of hierarchical microstructure features (γ, γ-twin, ε, ε-twin, and α′-variants) due to the co-activation of multiple deformation mechanisms has significantly contributed to challenging the conventional strength-ductility balance at cryogenic temperatures. Upon subjecting specimens to deformation at room temperature and 223 K, Σ3-type deformation γ-twins were dominated across the <111> oriented grains. These γ-twin boundaries effectively impede dislocation glide, leading to an increase in strain hardening [9,10,15,47,57]. Below 223 K, the tensile-fractured 316L specimens exhibited a hierarchical triple-phase microstructure comprising γ-fcc, γ-twin, ε-hcp, ε-twin, and α′-martensite phases. Furthermore, nanoscale twinning was activated at high strain levels. These nanoscale twinned structures have the propensity to absorb and release dislocations along twin boundaries, thereby mitigating strain localization during deformation [58]. Consequently, the strength-ductility synergy of 316L stainless steel is improved at cryogenic temperatures. During the martensitic transformation ($\gamma \to \varepsilon \to \alpha'$), the intersection structures such as twins, deformation bands, stacking faults, and ε-ε intersections are considered ideal nucleation sites for α′-martensite [59,60]. As plastic deformation increases, the density of these potential sites increases, resulting in a large amount of α′-martensite generated at cryogenic temperatures.

Recently, heterogeneous microstructures have been suggested to optimize the synergy between strength and ductility across various alloy systems [36,37]. Hierarchical microstructures, including bimodal nanograins and nano-twins, have the capacity to bolster strength-ductility balance. Furthermore, the emergence of several α′-martensite variants can be ascribed to the activation of different slip

systems featuring high Schmidt factors within {111} γ-planes during deformation. Alongside the conventional γ/ε/α′ triple-phase microstructure, nanoscale γ-twins and (1 0 $\bar{1}$ 2) type ε-twins are also generated to accommodate the localise strain induced during martensitic transformation. The deformation-induced γ → ε martensitic transformation generates local shape strains due to shears along habit planes, leading to the nucleation of various structures at γ/ε interfaces. The primary shear for the γ → ε transformation and the secondary shear on the conjugate plane for the ε → α′ transformation is 19.5° (T/2). In contrast, (1 0 $\bar{1}$ 2) ε-twinning requires only 6.6°, significantly lower than T/2 shear. Additionally, the nucleation of α′-bcc martensite induces internal strain at the ε/α′ intersection due to its larger atomic volume compared to ε-martensite. Consequently, (1 0 $\bar{1}$ 2) ε-twinning acts as a supplementary mechanism to accommodate local strain mismatches during the γ → ε → α′ transformation. Further details on the formation of ε-twinning during martensitic transformation are available in our previously published papers [59]. Moreover, a significant reduction in the size of α′-martensite laths is observed with the progression of plastic deformation at 123 K and 77 K temperatures. Interestingly, α′-martensite nucleated inside γ-twin during one-step ($\gamma/\gamma_{twin} \rightarrow \alpha'$) transformation exhibited larger lath sizes than those formed during two-step transformations. The strength and toughness imparted by α′-martensite are strongly influenced by the size of the lath, as it exerts a dynamic Hall-Petch effect in 316L stainless steel due to severe grain refinement during cryogenic deformation. Thus, the generation of several new interfaces among the hierarchical γ/ε/α′ triple-phase resulted in enhanced strain-hardening behavior and an overall high strength-ductility balance at cryogenic temperatures.

The exceptional strength-ductility balance exhibited by SUS 316L stainless steel at cryogenic temperatures can ultimately be attributed to its sustained strain-hardening behavior. This behavior arises from the combined effects of various hierarchical microstructure formations, including ε, α′, and γ-twins, as well as multi-mode deformation mechanisms such as deformation twinning and martensitic transformations. Additionally, the sluggish kinetics of α-martensite during the initial stages of deformation have played a crucial role in delaying necking and enhancing the material's work-hardening capacity. The coexistence of these triple phase structures suggests that the thermodynamic stability of the γ-fcc, ε-hcp, and α′-bcc phases is close to each other. However, the quantitative estimation of the Gibbs free energies (G_γ, G_ε, $G_{\alpha'}$) of these triple phases are out of the scope for the present study.

5. Conclusion

The present investigation into the tensile properties of 316L austenitic stainless steel at cryogenic temperatures unveils the new insights into its exceptional strength-ductility synergy. Notably, an exceptional strength-ductility balance surpassing the 80 GPa% threshold was achieved at 77 K. EBSD analysis revealed a shift in the governing deformation mechanism from deformation twinning to martensitic transformation below 223 K, with a transition from the γ → ε to two-step γ → ε → α′ transformation at higher plastic strain levels. The stress-strain curves satisfy the Considère criterion, indicated delayed necking at cryogenic temperatures. At these temperatures, the Gibbs free energy difference between ε-martensite and γ-austenite approaching zero, resulting in slow martensite growth. The sluggish kinetics of α′-martensite during the initial stages of deformation contributed to delayed necking and sustained work-hardening behaviour. In summary, overcoming the conventional strength-ductility trade-off of 316L ASS at cryogenic temperatures is attributed to synergetic strain hardening response driven by the evolution of hierarchical γ/ε/α′ triple-phase structures and the dynamic Hall-Petch effect exerted by newly formed interfaces and refined α′-martensite during plastic deformation. Overall, this study not only enhances our understanding of the strength-ductility trade-off and the underlying mechanisms in 316L stainless steel under cryogenic conditions but also provides a clear pathway for optimizing all types of ASSs involving ε/α′ martensitic transformation for extreme environments.

Data availability

The data that support the findings of this study are available upon reasonable request from the corresponding author.

Declaration of competing interest

The authors declare that they have no known competing financial interests or personal relationships that could have appeared to influence the work reported in this paper.

Acknowledgments

The authors acknowledge the support from the Japan Society for the Promotion of Science (JSPS, 21H01659). A part of this work was supported by a Grant-in-Aid for Early-Career Scientists (23K13227) from the JSPS, Japan.

References

[1] Marshall P. Austenitic stainless steels : microstructure and mechanical properties. 1984. p. 431.
[2] Karthik Desu R, Krishnamurthy HN, Balu A, Kumar Gupta A, Singh SK. Mechanical properties of austenitic stainless steel 304L and 316L at elevated temperatures. https://doi.org/10.1016/j.jmrt.2015.04.001; 2015.
[3] Karjalainen LP, Taulavuori T, Sellman M, Kyröläinen A. Some strengthening methods for austenitic stainless steels. Steel Res Int 2008;79:404–12. https://doi.org/10.1002/SRIN.200806146.
[4] Ohkubo I, Miyakusu K, Uematsu Y, Kimura H. Effect of alloying elements on the mechanical properties of the stable austenitic stainless steel. ISIJ Int 1994;34:764–72. https://doi.org/10.2355/ISIJINTERNATIONAL.34.764.
[5] Singh D, Gatey AM, Devan RS, Antunes V, Alvarez F, Figueroa CA, et al. Surface treatment response of AISI 2205 and AISI 304L steels: SMAT and plasma-nitriding. Surf Eng 2019;35:205–15. https://doi.org/10.1080/02670844.2018.1516372.
[6] Singh D, Basha DA, Singh A, Devan RS, Hosmani SS. Microstructural and passivation response of severely deformed AISI 304 steel surface: the role of surface mechanical attrition treatment. J Mater Eng Perform 2020;29:6898–911. https://doi.org/10.1007/s11665-020-05161-6.
[7] Ding J, Zhang L, Li D, Lu M, Xue J, Zhong W. Corrosion and stress corrosion cracking behavior of 316L austenitic stainless steel in high H2S-CO2-Cl-environment. J Mater Sci 2013;48:3708–15. https://doi.org/10.1007/S10853-013-7168-1/FIGURES/9.
[8] Fajobi MA, Loto RT, Oluwole OO. Austenitic 316L stainless steel; corrosion and organic inhibitor: a review. Key Eng Mater 2021;886:126–32. https://doi.org/10.4028/WWW.SCIENTIFIC.NET/KEM.886.126.
[9] Galindo-Nava EI, Rivera-Díaz-del-Castillo PEJ. Understanding martensite and twin formation in austenitic steels: a model describing TRIP and TWIP effects. Acta Mater 2017;128:120–34. https://doi.org/10.1016/J.ACTAMAT.2017.02.004.
[10] Pham MS, Dovgyy B, Hooper PA. Twinning induced plasticity in austenitic stainless steel 316L made by additive manufacturing. Mater Sci Eng, A 2017;704:102–11. https://doi.org/10.1016/J.MSEA.2017.07.082.
[11] Song RB, Xiang JY, Hou DP. Characteristics of mechanical properties and microstructure for 316L austenitic stainless steel. J Iron Steel Res Int 2011;18:53–9. https://doi.org/10.1016/S1006-706X(11)60117-9.
[12] Sinha S, Szpunar J, Kumar NAPK, Gurao NP. Tensile deformation of 316L austenitic stainless steel using in-situ electron backscatter diffraction and crystal plasticity simulations. Mater Sci Eng, A 2015;637:48–55. https://doi.org/10.1016/j.msea.2015.04.005.
[13] Ban H, Shi G. A review of research on high-strength steel structures. Https://DoiOrg/101680/Jstbu16001972018;vol. 171:625–641.
[14] Takahashi M. Development of high strength steels for automobiles. Nippon Steel 2003;. 88:2–7.
[15] Bouaziz O, Allain S, Scott CP, Cugy P, Barbier D. High manganese austenitic twinning induced plasticity steels: a review of the microstructure properties relationships. Curr Opin Solid State Mater Sci 2011;15:141–68. https://doi.org/10.1016/J.COSSMS.2011.04.002.
[16] Li S, Withers PJ, Kabra S, Yan K. The behaviour and deformation mechanisms for 316L stainless steel deformed at cryogenic temperatures. Mater Sci Eng, A 2023;880. https://doi.org/10.1016/j.msea.2023.145279.
[17] Cheng W, Cui D, Sun Y, Liu W, Xu Y, Liu B. Cryogenic work-hardening behavior for a metastable austenitic stainless steel at liquid nitrogen temperature. Mater Sci Eng, A 2022;861. https://doi.org/10.1016/j.msea.2022.144352.
[18] Larbalestier DC, King HW. Austenitic stainless steels at cryogenic temperatures 1-Structural stability and magnetic properties. Cryogenics 1973;13:160–8. https://doi.org/10.1016/0011-2275(73)90285-3.

[19] Nguyen LTH, Hwang JS, Kim MS, Kim JH, Kim SK, Lee JM. Charpy impact properties of hydrogen-exposed 316l stainless steel at ambient and cryogenic temperatures. Metals 2019;9. https://doi.org/10.3390/met9060625.
[20] Tang L, Magdysyuk OV, Jiang F, Wang Y, Evans A, Kabra S, et al. Mechanical performance and deformation mechanisms at cryogenic temperatures of 316L stainless steel processed by laser powder bed fusion: in situ neutron diffraction. Scripta Mater 2022;218. https://doi.org/10.1016/j.scriptamat.2022.114806.
[21] Han G, He J, Fukuyama S, Yokogawa K. Effect of strain-induced martensite on hydrogen environment embrittlement of sensitized austenitic stainless steels at low temperatures. Acta Mater 1998;46:4559–70. https://doi.org/10.1016/S1359-6454(98)00136-0.
[22] McHenry HI. The properties of austenitic stainless steel at cryogenic temperatures. Austenitic Steels at Low Temperatures 1983:1–27. https://doi.org/10.1007/978-1-4613-3730-0_1.
[23] He Y, Gao J, He Y, Shin K. A new fcc-bcc orientation relationship observed in the strain-induced martensitic transformation of an austenitic stainless steel. Mater Lett 2021;305. https://doi.org/10.1016/j.matlet.2021.130735.
[24] Man J, Obrtlík K, Petrenec M, Beran P, Smaga M, Weidner A, et al. Stability of austenitic 316L steel against martensite formation during cyclic straining. Procedia Eng 2011;10:1279–84. https://doi.org/10.1016/j.proeng.2011.04.213. Elsevier Ltd.
[25] Staudhammer KP, Murr LE, Hecker SS. Nucleation and evolution of strain-induced martensitic (b.c.c.) embryos and substructure in stainless steel: a transmission electron microscope study. Acta Metall 1983;31:267–74. https://doi.org/10.1016/0001-6160(83)90103-7.
[26] Xiong Y, He T, Lu Y, Ren F, Volinsky AA, Cao W. Tensile deformation temperature impact on microstructure and mechanical properties of AISI 316LN austenitic stainless steel. J Mater Eng Perform 2018;27:1232–40. https://doi.org/10.1007/s11665-018-3234-9.
[27] Nalepka K, Skoczeń B, Ciepielowska M, Schmidt R, Tabin J, Schmidt E, et al. Phase transformation in 316l austenitic steel induced by fracture at cryogenic temperatures: experiment and modelling. Materials 2021;14:1–27. https://doi.org/10.3390/ma14010127.
[28] Spencer KK, Véron M, Zhang Y, Embury JD. The strain induced martensite transformation in austenitic stainless steels Part 1 - influence of temperature and strain history. Mater Sci Technol 2009;25:7–17. https://doi.org/10.1179/174328408X293603.
[29] Solomon N, Solomon I. Deformation induced martensite in AISI 316 stainless steel. Rev Metal (Madr) 2010;46:121–8. https://doi.org/10.3989/revmetalm.0920.
[30] Byun TS, Lee EH, Hunn JD. Plastic deformation in 316LN stainless steel - characterization of deformation microstructures. J Nucl Mater 2003;321:29–39. https://doi.org/10.1016/S0022-3115(03)00195-8.
[31] Ma Y, Naeem M, Zhu L, He H, Sun X, Yang Z, et al. Microscopic insights of the extraordinary work-hardening due to phase transformation. Acta Mater 2024;270. https://doi.org/10.1016/j.actamat.2024.119822.
[32] Hamada AS, Karjalainen LP, Misra RDK, Talonen J. Contribution of deformation mechanisms to strength and ductility in two Cr-Mn grade austenitic stainless steels. Mater Sci Eng, A 2013;559:336–44. https://doi.org/10.1016/j.msea.2012.08.108.
[33] Romero-Resendiz L, El-Tahawy M, Zhang T, Rossi MC, Marulanda-Cardona DM, Yang T, et al. Heterostructured stainless steel: properties, current trends, and future perspectives. Mater Sci Eng R Rep 2022;150:100691. https://doi.org/10.1016/J.MSER.2022.100691.
[34] Wei Y. Evading the strength–ductility trade-off dilemma in steel through gradient hierarchical nanotwins. Nat Commun 2014;5. https://doi.org/10.1038/ncomms4580.
[35] Lu K. Making strong nanomaterials ductile with gradients: microstructures that increase metal crystallite size from nanoscale with surface depth are both strong and ductile. Science 2014;345:1455–6. https://DOI:10.1126/science.125594.
[36] Li Y, Li W, Li S, Min N, Jiang L, Zhou Q, et al. Ensuring the strength and ductility synergy in an austenitic stainless steel: single- or multi-phase hetero-structures design. Scripta Mater 2021;193:81–5. https://doi.org/10.1016/J.SCRIPTAMAT.2020.10.041.
[37] Zheng R, Liu M, Zhang Z, Ameyama K, Ma C. Towards strength-ductility synergy through hierarchical microstructure design in an austenitic stainless steel. Scripta Mater 2019;169:76–81. https://doi.org/10.1016/J.SCRIPTAMAT.2019.05.017.
[38] Yan FK, Liu GZ, Tao NR, Lu K. Strength and ductility of 316L austenitic stainless steel strengthened by nano-scale twin bundles. Acta Mater 2012;60:1059–71. https://doi.org/10.1016/J.ACTAMAT.2011.11.009.
[39] Li J, Cao Y, Gao B, Li Y, Zhu Y. Superior strength and ductility of 316L stainless steel with heterogeneous lamella structure. J Mater Sci 2018;53:10442–56. https://doi.org/10.1007/S10853-018-2322-4.
[40] Liu J, Jin Y, Fang X, Chen C, Feng Q, Liu X, et al. Dislocation strengthening without ductility trade-off in metastable austenitic steels. https://doi.org/10.1038/srep35345; 2016.
[41] Zheng C, Yu W. Effect of low-temperature on mechanical behavior for an AISI 304 austenitic stainless steel. Mater Sci Eng, A 2018;710:359–65. https://doi.org/10.1016/j.msea.2017.11.003.
[42] Datta K, Delhez R, Bronsveld PM, Beyer J, Geijselaers HJM, Post J. A low-temperature study to examine the role of ε-martensite during strain-induced transformations in metastable austenitic stainless steels. Acta Mater 2009;57:3321–6. https://doi.org/10.1016/j.actamat.2009.03.039.
[43] Seetharaman V, Krishnan R. Influence of the martensitic transformation on the deformation behaviour of an AISI 316 stainless steel at low temperatures, vol. 16; 1981.
[44] Saenarjhan N, Kang JH, Kim SJ. Effects of carbon and nitrogen on austenite stability and tensile deformation behavior of 15Cr-15Mn-4Ni based austenitic stainless steels. Mater Sci Eng, A 2019;742:608–16. https://doi.org/10.1016/j.msea.2018.11.048.
[45] Lou S. Effect of temperature on the lower yield strength and static strain ageing in low-carbon steels. J Mater Sci 1995;30:1434–8. https://doi.org/10.1007/BF00375244.
[46] Soleimani M, Kalhor A, Mirzadeh H. Transformation-induced plasticity (TRIP) in advanced steels: a review. Mater Sci Eng, A 2020;795:140023. https://doi.org/10.1016/j.msea.2020.140023.
[47] Koyama M, Sawaguchi T, Tsuzaki K. TWIP Effect and plastic instability condition in an Fe-Mn-C austenitic steel. ISIJ Int 2013;53:323–9. https://doi.org/10.2355/isijinternational.53.323.
[48] Gnäupel-Herold T, Creuziger A. Diffraction study of the retained austenite content in TRIP steels. Mater Sci Eng, A 2011;528:3594–600. https://doi.org/10.1016/j.msea.2011.01.030.
[49] Wang W, Yan W, Yang K, Shan Y, Jiang Z. Temperature dependence of tensile behaviors of nitrogen-alloyed austenitic stainless steels. J Mater Eng Perform 2010;19:1214–9. https://doi.org/10.1007/s11665-010-9603-7.
[50] Masumura T, Tsuchiyama T, Takaki S, Koyano T, Adachi K. Difference between carbon and nitrogen in thermal stability of metastable 18%Cr-8%Ni austenite. Scripta Mater 2018;154:8–11. https://doi.org/10.1016/j.scriptamat.2018.05.019.
[51] Lee Y-K, Choi C-S. Driving force for → martensitic transformation and stacking fault energy of in Fe-Mn binary system. Metall Mater Trans A 2000;31:355–60. https://doi.org/10.1007/s11661-000-0271-3.
[52] Molnár D, Sun X, Lu S, Li W, Engberg G, Vitos L. Effect of temperature on the stacking fault energy and deformation behaviour in 316L austenitic stainless steel. https://doi.org/10.1016/j.msea.2019.05.079; 2019.
[53] Gutierrez-Urrutia I, Raabe D. Dislocation and twin substructure evolution during strain hardening of an Fe–22 wt.% Mn–0.6 wt.% C TWIP steel observed by electron channeling contrast imaging. Acta Mater 2011;59:6449–62. https://doi.org/10.1016/J.ACTAMAT.2011.07.009.
[54] Olson GB, Cohen M. A general mechanism of martensitic nucleation: Part I. General concepts and the FCC → HCP transformation. Metall Trans A 1976;7:1897–904. https://doi.org/10.1007/BF02659822/METRICS.
[55] Curtze S, Kuokkala VT, Oikari A, Talonen J, Hänninen H. Thermodynamic modeling of the stacking fault energy of austenitic steels. Acta Mater 2011;59:1068–76. https://doi.org/10.1016/J.ACTAMAT.2010.10.037.
[56] Yonezawa T, Suzuki K, Ooki S, Hashimoto A. The effect of chemical composition and heat treatment conditions on stacking fault energy for Fe-Cr-Ni austenitic stainless steel. Metall Mater Trans A 2013;44:5884–96. https://doi.org/10.1007/s11661-013-1943-0.
[57] Galindo-Nava EI, Rivera-Díaz-del-Castillo PEJ. Understanding martensite and twin formation in austenitic steels: a model describing TRIP and TWIP effects. Acta Mater 2017;128:120–34. https://doi.org/10.1016/J.ACTAMAT.2017.02.004.
[58] Dao M, Lu L, Shen YF, Suresh S. Strength, strain-rate sensitivity and ductility of copper with nanoscale twins. Acta Mater 2006;54:5421–32. https://doi.org/10.1016/J.ACTAMAT.2006.06.062.
[59] Singh D, Tasaki W, Yoshinaka F, Takamori S, Emura S, Tsuchiya K, et al. Unveiling the transformation pathways of hierarchical γ90 – εtwin – α' triple phase structure formation at ε-ε martensite intersection. Mater Char 2023;205:113358. https://doi.org/10.1016/J.MATCHAR.2023.113358.
[60] Lee TH, Ha HY, Kang JY, Moon J, Lee CH, Park SJ. An intersecting-shear model for strain-induced martensitic transformation. Acta Mater 2013;61:7399–410. https://doi.org/10.1016/j.actamat.2013.08.046.